Available online at www.sciencedirect.com
ScienceDirect
International Journal of Mass Spectrometry 269 (2008) 12–23
International Journal of Mass Spectrometry
www.elsevier.com/locate/ijms

Characterization of a new open cylindrical ICR cell for ion–ion collision studies☆

Basem Kanawati*, Karl Peter Wanczek

Department of Physical and Inorganic Chemistry, University of Bremen, Bremen, Germany

Received 28 May 2007; accepted 4 September 2007
Available online 21 September 2007

Abstract

Experiments were done in a new open cylindrical ICR cell to establish ion–ion collisions between positive and negative ions of SF_6 in the gas phase for the first time. Only one electron pulse for ion generation was employed (single shot). The role of pressure was illustrated to encourage high ion densities to be a prerequisite for ion–ion reactions. No electron transfer could be deduced from the experiments. Anion–anion collisions could be indicated. The dynamics of applied potential changes on both ion polarities in a double well potential configuration was studied intensively. In depth analysis of radial excitation patterns of positive and negative ions trapped simultaneously in different stability regions reveals sharp discrimination in the extent of radial acceleration. SIMION simulations were done to probe several electric forces, which both positive and negative ions experience during radial excitation event. Axial component of radial dipolar excitation field was also analyzed. Distortion in radial ion trajectories during radial excitation event was indicated when both ion polarities were excited simultaneously.

Keywords: Ion–ion collision; ICR; SIMION trajectory; Potential distribution; Radial axial motion

1. Introduction

Fourier transform ion cyclotron resonance FT-ICR [1] mass spectrometry is based on a 3D ion confinement by use of a static homogeneous high magnetic field combined with an axial quadrupolar electrostatic trapping potential. The ICR technique does not only provide the highest mass resolving power in the world of mass spectrometry, it also acts as a gas phase electronic reactor to study ion-molecule reactions [2–4] and ionic fragmentation mechanisms, induced upon collisional activation of kinetically accelerated ions. Several ion manipulations such as mass-selective excitation/ejection, quadrupolar axialization [5–7] and ion transfer between adjacent compartments of the ICR cell were implemented.

Different ICR cell geometries were studied in the past [8–10]. Guan and Marshall have written a review [11] of ion traps for FT-ICR mass spectrometry and they discussed the electric configurations in a closed cubic and open cylindrical cell.

Although Penning traps [12,13] are able to produce the most ideal quadrupolar axial and radial potential forms, they are limited to the study of one ion polarity. Extending ICR capability to trap both ion polarities simultaneously was achieved by use of nested cells in a static electric field [14–17]. However, previous geometries of nested ICR cells, which are operated under double well potential configuration, provided a main central stability region for one ion polarity inside the detection region and two terminal ion stability regions for the other polarity outside and near the detection region. This leads to discrimination in ion detection between positive and negative ions.

Dynamic ion trapping was also implemented in closed cubic [18] and open cylindrical [19] geometries. However, the trapping efficiency in axial direction depends on the m/z ratio in the RF operation mode and the simultaneous trapping of positive and negative ions under RF electric field in ICR is only possible in a reduced mass window. Furthermore, simultaneous radial excitation and detection of both ion polarities will induce unfavourable noise in the detection circuit especially for large

☆ Address reprint requests to Prof. Dr. Karl Peter Wanczek, University of Bremen, NW2, A0090, D-28334 Bremen, Germany.
* Corresponding author at: Max-Planck-Institute for Chemistry, Atmospheric Chemistry Division, Joh., Joachim Becherweg 27, D-55128 Mainz, Germany.
E-mail addresses: kanawati@t-online.de, Kanawati.B@gmail.com (B. Kanawati), icrwan@icr.uni-bremen.de (K.P. Wanczek).
URL: http://www.kanawati.de (B. Kanawati).

1387-3806/$ – see front matter © 2007 Elsevier B.V. All rights reserved.
doi:10.1016/j.ijms.2007.09.007

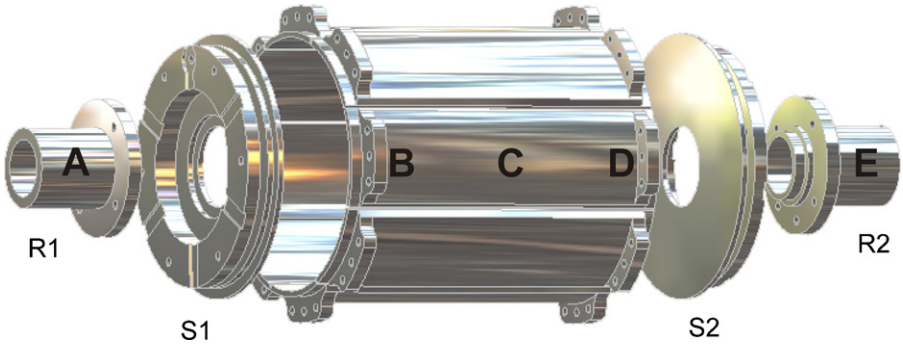

Fig. 1. 3D exploded view for the new ICR cell. The cell has five different regions for trapping positive and negative ions, because the cell is located in a grounded ICR-tube (not shown here). Detection is possible only inside the region from B to D along C. VESPEL isolation plates are not shown for clarity.

ions if the RF-trapping field has to be dominant during the excitation event. If no RF trapping field exists, only one ion polarity can be radially excited and thus detected.

Although ion–ion electron transfer dissociation experiments remain confined to RF Paul traps [20], antiproton–positron recombinations were implemented by Gabrielse et al. [21] in ICR. Electron capture dissociation (ECD), which implies recombination of positive ions with low energy electrons in the gas phase, discovered by Zubarev et al. [22], is another interesting subject, which could be achieved experimentally in the ICR cell.

In this paper, we introduce a new cell geometry, which is not only capable of trapping and detecting positive and negative ion simultaneously, but it is also able to separate those ions radially from each other. The effective electric potential in this cell is higher than that of traditional open cylindrical cell geometry at the same applied voltage. Three ion stability regions exist inside (not outside and near) the region, where radial excitation and detection can take place. This cell combines the advantages of both closed and open cell geometries. It has open tube electrodes, which allow for efficient pumping and make the cell compatible with external ionization sources. In comparison with the terminal ion stability regions, the axial component of the radial dipolar electric field is small especially in the central stability region.

The cell has several trapping electrodes with different shapes which allow for double well potential configuration to be applied for simultaneous trapping and detection of both ion polarities. Beside intensive characterization of such a double well potential configuration, new operation modes were developed to induce axial ion–ion collisions, not only between different ion polarities but also between same ion polarities (such as anion–anion collisions). These operation modes were studied theoretically and implemented experimentally. Discrimination in ion detection depending on the ion polarity was also observed in this new cell geometry and is described.

2. Experimental

For all experimental investigations a prototype FT-ICR spectrometer Bruker CMS 47X was employed, equipped with a 7 T superconducting magnet with 89 mm room temperature bore. A UHV system connected with two fine vacuum gas inlet systems at base pressures of 3×10^{-2} mbar was used. With a turbo molecular pump of 240 L/s pumping speed (Pfeiffer) connected to a rotary pump the UHV-system could reach base pressure of 1×10^{-9} mbar. The sample pressure was kept constant at 2×10^{-7} mbar for experiments shown in Fig. 2 and at 2×10^{-6} mbar for experiments shown in Fig. 4 in Section 3.2.

The new ICR cell is described in detail elsewhere [23]. Therefore here only a short description will be given. Fig. 1 shows a 3D exploded view of the ICR cell. R1, R2 are two stainless steel tube electrodes with an inner diameter of 10 mm and 2 mm wall thickness. Each tube electrode is 20 mm long. S1 and S2 are side electrodes, which have a circular geometry with a hole of 14 mm inner diameter in the center of each in order to be compatible with the tube electrodes R1 and R2 mentioned above for installation. Outer diameter of the side electrode is 44 mm. The inner length of the ring electrodes between S1 and S2 is 60 mm. The ring electrodes consist of eight stainless steel segments with each two segments wired together. This way, ion detection sensitivity and excitation electric field strength are increased and the ICR cell runs at dipolar excitation and dipolar detection. VESPEL isolation material (not shown for clarity) was used to electrically isolate the different neighbouring electrodes from each other. This material does not degas, when the UHV system is heated to 250 °C during the pumping period to achieve lower pressure values.

The inner diameter of the ICR-cell is 46 mm. The whole ICR cell assembly is surrounded with a grounded stainless steel tube with an inner diameter of 82 mm. The convention 1/6/0/6/1 for example means that tube electrodes R1 and R2 are at +1 V each and the side electrodes S1 and S2 have +6 V each relative to the grounded ring electrodes (eight segments), which are located in the central region of the ICR cell. In this way, trapping of positive ions in the terminal regions A and E is not possible. This is desirable, since ions trapped there cannot be detected. Furthermore positive ions in regions A and E cannot be accelerated toward the center of the ICR cell by pulsing different voltages on both tube electrodes R1 and R2 relative to the grounded eight segments of ring electrodes within the potential range (−9 to +9) V, that can be controlled from the DAC card, which delivers a potential channel for each tube and side electrode.

Using the above-mentioned double hill potential configuration, positive ions can be trapped only in the central region C (central trapping), while negative ions are trapped on both potential hills in regions B and D (terminal trapping). This potential configuration has proven to be suitable for efficient detection of

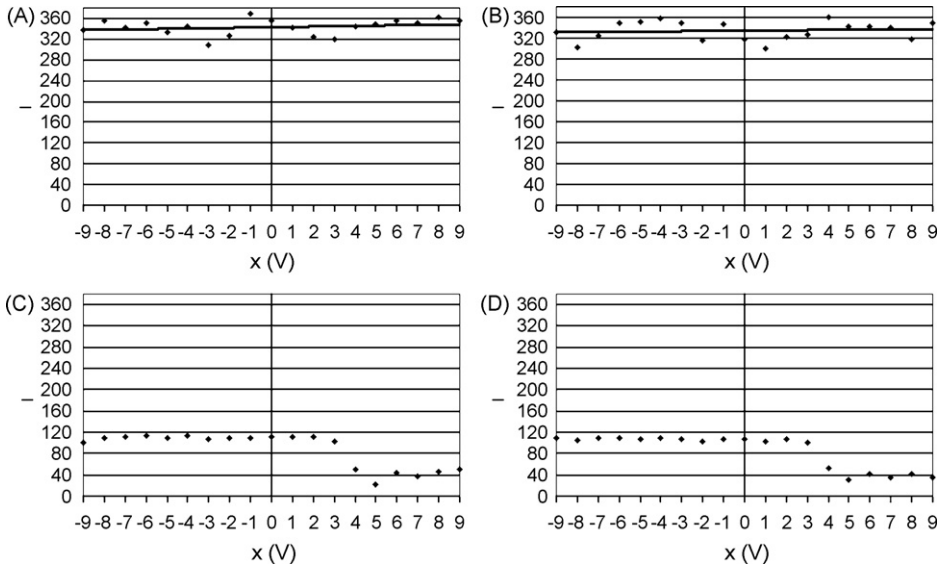

Fig. 2. Signal intensity vs. tube potentials x in the potential configuration x/6/0/6/x at 2×10^{-7} mbar. (A) SF_3^+ ions trapped alone, (B) SF_3^+ ions trapped together with SF_6^-, (C) SF_6^- ions trapped alone and (D) SF_6^- ions trapped simultaneously with SF_3^+ ions.

both polarities simultaneously, although it is not so efficient to provide high detection sensitivity toward negative ions trapped in the terminal regions B and D, when positive ions are trapped in the center simultaneously.

The experiments described in Section 3.1 were done with sulfur hexafluoride. The base peak in the spectrum, SF_5^+, was quenched since the intention of the authors was to demonstrate interactions between ion polarities in the mixture (SF_3^+/SF_6^-).

Three experiments were done to produce the results shown in Figs. 2 and 4 in Section 3.1.

In the first experiment, only SF_3^+ ions were studied in the central region of the ICR cell with absence of other positive and negative ions. Results are shown in diagram A of Figs. 2 and 4.

In the second experiment, only SF_6^- ions were studied in the terminal regions B and D of the cell. Results are shown in diagram C in Figs. 2 and 4.

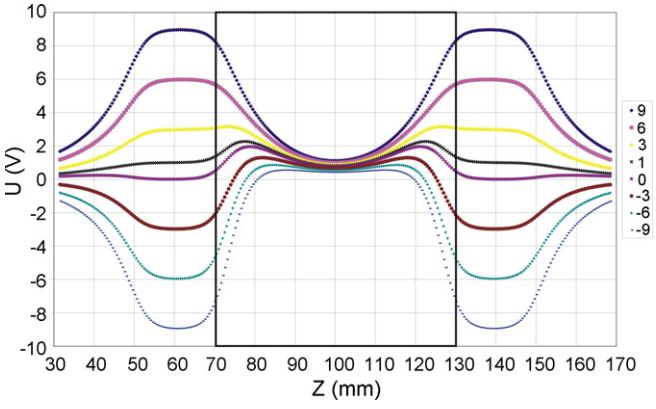

Fig. 3. Axial potential curves in the potential configuration x/6/0/6/x, where x is the potential of each tube electrode R1 and R2. x values are shown in the legend at the right side of the diagram. Axial segments are as follows: R1(50–70) mm, detection region between side electrodes S1 and S2 (70–130) mm, R2(130–150) mm. Detection region is surrounded by a black rectangle.

In the third experiment, both SF_3^+ and SF_6^- were trapped and detected simultaneously. Results are shown in diagrams B and D in Figs. 2 and 4.

All ions from SF_6 molecules were trapped after the end of the ionization pulse at the static double hill potential configuration 1/6/0/6/1 for 1 s to allow for axial collisional ion damping, before SF_5^+ ions and other unwanted ions (if necessary) were radially excited for ejection.

1/6/0/6/1 characterizes the following potential configuration: V(R1) = 1 V, V(S1) = 6 V, V(BCD) = 0 V, V(S2) = 6 V, V(R1) = 1 V. Radial ejection was done with on-resonance dipolar radial excitation RF pulses.

After the end of ejection pulses, a DAC card, which controls that potential of tube electrodes R1 and R2 was externally triggered by a pulse from the console to the DAC card installed on a separate computer to allow for altering the tube potentials from +1 V to the value x for just a fixed duration of 1 ms before setting back the tube potentials to +1 V again at R1 and R2 electrodes.

After the end of this DAC interference on both tube electrodes, an additional 100 ms delay time was allowed before all ions were radially excited for detection in the static potential configuration 1/6/0/6/1.

An automation program was written for the Aspect computer to control the experimental events inside the ICR cell. The logical sequence of this program is as follows.

The ionization electron beam duration was 25 ms for experiments shown in Fig. 4 (2×10^{-6} mbar) and 200 ms for experiments shown in Fig. 2 (2×10^{-7} mbar). The kinetic energy of electrons was 70 eV. Electrons were gated using a triggered gate located between the filament and the ICR cell. The gate potential was set up to be −60 V during the ionization pulse to allow electrons to be accelerated with +10 eV toward the gate and then pass to the ICR cell, while the gate potential was −109 V in the closed mode. This kind of experiment is called "single shot" experiment.

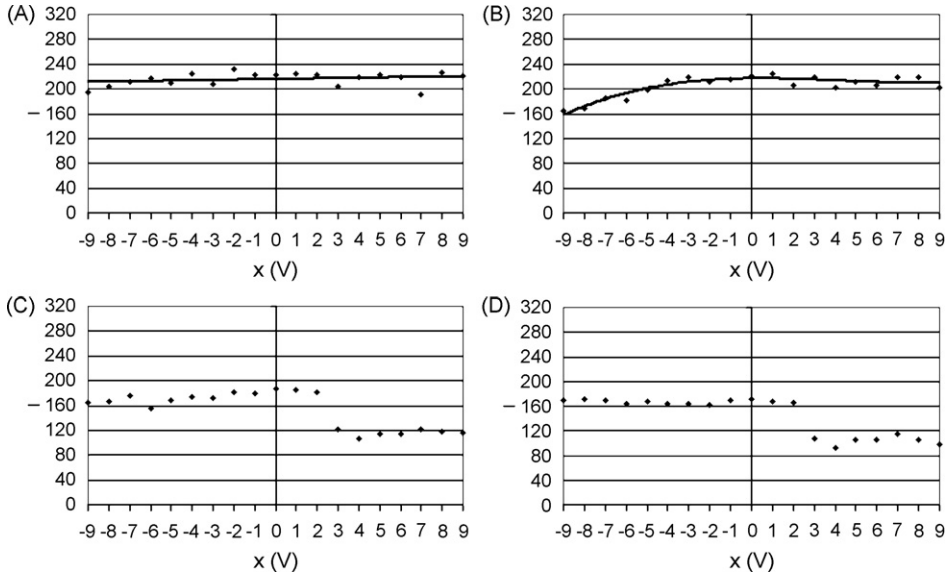

Fig. 4. Dependence of ion signal intensities on the potential value of each tube electrode along the potential configuration *x*/6/0/6/*x* at 2×10^{-6} mbar. (A) SF_3^+ ions trapped alone, (B) SF_3^+ ions trapped together with SF_6^- simultaneously, (C) SF_6^- ions trapped alone and (D) SF_6^- ions trapped simultaneously with SF_3^+ ions, as in Fig. 2.

The distance between the electron gate and the terminal tube of the ICR cell is 70 mm. This was sufficient to eliminate any interference of external electric fields generated from the gate itself on the potential configuration set up inside the ICR cell. Thus no gate influence exists on ion trajectories inside the ICR cell.

3. Results and discussion

3.1. Axial motion of the ions

3.1.1. Axial single shot experiments run at different voltages of tube electrodes in the mixture (SF_3^+/SF_6^-) in initial potential configuration 1/6/0/6/1

In the double hill potential configuration 1/6/0/6/1 SF_3^+ and SF_6^- ions were trapped (as discussed above) and detected simultaneously. SF_5^+ ions (the base peak in EI spectrum of SF_6 gas) was quenched using one radial on resonance single shot pulse triggered directly after a post-ionisation delay time of 1 s. This post-ionisation delay time was set up deliberately to ensure that collisional damping of both positive and negative ions took place so that each ion polarity relaxed in its corresponding stability region.

After the end of the radial ejection pulse, the potential of each tube electrode R1 and R2 was varied to a value of *x* V on both tube electrodes simultaneously for 1 ms duration, before the potential configuration was then set back to 1/6/0/6/1 again. Thus the progression of potential parameters is as follows: 1/6/0/6/1 >➡ x/6/0/6/x > ➡ 1/6/0/6/1

The SIMION simulations described below, show the possibility of spatial anion exchange and positive/negative ion–ion collision inside the ICR cell using the potential change scheme for one time (axial single shot).

Fig. 2 shows signal intensity dependences of positive and negative ions trapped in different regions in the ICR cell as a function of the potential *x* of each tube electrode in the potential configuration *x*/6/0/6/*x* at a pressure of 2×10^{-7} mbar. As shown in diagrams A and B, no difference of SF_3^+ behaviour can be noticed. Central SF_3^+ ions remain trapped in the ICR cell even if the potential of each tube electrode is set to −9 V. This is due to the presence of a very flat potential well in central region C of the cell, which is capable to trap all SF_3^+ ions generated as fragments ions from electron impact ionisation of SF_6 neutrals.

On the other hand, a sharp drop in SF_6^- signal intensity is experimentally observed for *x* potentials above +3 V, regardless of the fact, whether SF_3^+ ions were simultaneously trapped or not (see diagrams C and D in Fig. 2). This is due to the outward directed force, which arises from the potential change: from the initial configuration 1/6/0/6/1 to the transit configuration *x*/6/0/6/*x* for $x > +3$ V on both tube electrodes (as shown Fig. 3). This force applies on the terminal SF_6^- ions trapped in regions B and D and attracts them to the outer electrodes. The terminal potential maxima shift in the same direction. Details will be discussed in the simulations shown later.

However, SF_6^- ions could still be detected for $x > +3$ V, since terminal potential hills still exist in the extreme terminal regions A and E. In regions A and E detection is not possible, because only the ring electrode BCD is connected to the detector. That SF_6^- can still be detected is explained as follows: electric potential hills exist even for tube electrode potentials $x > 3$ V, since the ICR cell is surrounded by a grounded ICR vacuum tube. Thus, potentials outside the ICR cell tend to reach 0 V along the *z*-axis. This establishes symmetrical double hill potential configuration, where negative ions vibrate in the terminal regions A and E. However, those negative ions with higher translational energies have higher trapping amplitudes and they spend greater times

at both reversal points of axial vibrations. One of these reversal points is located inside the detection terminal regions B and D, and this justifies detection of some SF_6^- ions for $x > +3$ V.

From Fig. 2, no evidence for ion–ion collisions can be deduced. However, running the same experiments at a higher pressure (2×10^{-6} mbar), shows the influence of SF_6^- ion spatial exchange on the observed signal intensity of SF_3^+ in the potential range $-9 < x < +9$ V in the transit potential configuration $x/6/0/6/x$ (Fig. 4). Fig. 4 shows a remarkable drop in the signal intensity of SF_6^- ions for $x > +3$ V, regardless of whether SF_3^+ ions were also trapped in the central region or not. This was also observed before in Fig. 2. Shifts of terminal anion stability regions of the double hill potential curve toward the outer sides of the ICR cell are responsible for this observation.

On the other hand, we realize from the experiments run at higher pressure (2×10^{-6} mbar in Fig. 4), that there is a noticeable drop in the signal intensity of SF_3^+ ions too, when SF_6^- ions are trapped simultaneously at anion spatial exchange conditions ($x < -4$ V). This indicates ion–ion collisions between axially excited SF_6^- ions and central SF_3^+ ions. It should be emphasized, that SF_3^+ ions are stable for x values in the range $(-4 > x > -9)$ V at the same pressure, when SF_6^- ions are absent (diagram A in Fig. 4). This indicates the existence of a central stability region for positive ions even at high negative tube potentials. Thus, the noticeable drop in the signal intensity of SF_3^+ with the presence of axially excited SF_6^- for $x < -4$ V in diagram B of Fig. 4 is an experimental evidence of the SF_6^- ion influence on SF_3^+ ions during ion-ion collisions. The experiments shown in Fig. 4 show the role of a high pressure in increasing ion densities of both polarities and thus increasing the collision probability.

As the pressure increases from 2×10^{-7} to 2×10^{-6} mbar, SF_6^- ion signal intensity increases from 100 to over 160, while SF_3^+ ion signal intensity decreases from 340 to 220 units, if each ion polarity is trapped alone (with the absence of the other ion polarity). It should be mentioned, that the ionisation pulse duration was 25 ms at 2×10^{-6} mbar and 200 ms at 2×10^{-7} mbar.

However, the noticeable decrease in the ion signal intensity of SF_3^+ (in the absence of SF_6^-) as the pressure increases indicates oversaturation in positive ion concentrations in the central stability region (ion–ion columbic repulsion) in addition to the role of the outward directed radial electric field, which applies on positive ions trapped in the central region (see below).

Fig. 5 shows the maximum effective potential in region B of the ICR cell as a function of the potential of each tube electrode R1 and R2 in the potential configuration $x/6/0/6/x$. From Fig. 5 it is clear that the effective local potential maximum does not rise linearly, but exponentially as a function of the potential of each tube electrode x.

Within the potential transition from 1/6/0/6/1 to 9/6/0/6/9 SF_6^- ions can gain up to 6.7 eV kinetic energy in the outward directed acceleration accompanied with this potential change. On the other hand, a potential transition from the initial configuration 1/6/0/6/1 to −9/6/0/6/−9 accelerates terminal negative ions toward the center of the ICR cell with a kinetic energy of 1.7 eV only, if no collisions between the accelerated ions and neutrals are to be considered.

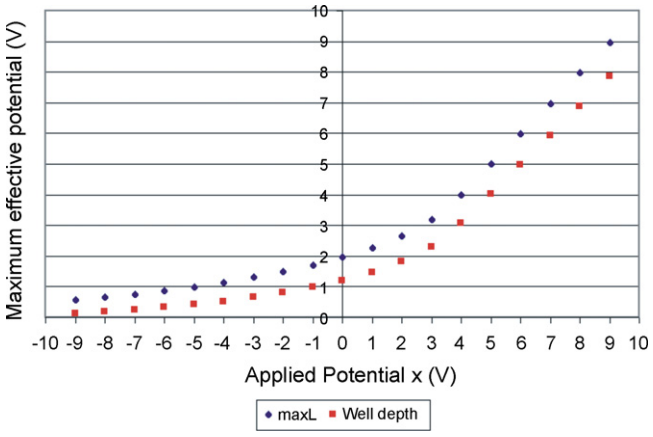

Fig. 5. The effective potential value of the left maximum (maxL) in the potential configuration $x/6/0/6/x$ as a function of applied potentials x on both tube electrodes R1 and R2. Well depth values in the central region C of the ICR cell are also shown.

Let us explain, why do SF_6^- ions still remain trapped inside the cell, even if they are inward-accelerated axially by the potential change from initial configuration 1/6/0/6/1 to −9/6/0/6/−9.

The maximum kinetic energy gain for terminal axially accelerated SF_6^- ions toward the center of the cell without collision effects is low (1.7 eV) as seen from Fig. 5 previously. The potential configuration −9/6/0/6/−9 shown in Fig. 3 reveals an energy barrier of 8.4 eV between the local minimum potential well at $Z = 60$ mm and its corresponding local maximum at $Z = 87.5$ mm. This high potential barrier could not be overcome by axially accelerated SF_6^- ions, which have maximum kinetic energy of just 1.7 eV. The effective kinetic energy acquired by terminal negative ions during axial acceleration is even lower than 1.7 eV due to high collision frequencies with SF_6 neutrals at high pressures. This justifies why SF_6^- ion loss has not been experimentally observed even at low tube potential values of −9 V in the transit potential configuration $x/6/0/6/x$. Thus, this strategy of potential change of both tube electrodes accelerates terminal SF_6^- ions toward the cell center and leads to a spatial anion exchange without axial ejection of negative ions out of the ICR cell.

The electron affinity of SF_6 is just 1.1 eV. The potential change described above provides 1.7 eV more kinetic energy to the initially thermal terminal SF_6^- ions. The accelerated SF_6^- ions have energies above threshold and could loose an electron and produce a noticeable loss in the signal intensity of SF_6^- ions. This was not observed. In addition, no fragment ions (such as SF_5^-) were observed due to this axial acceleration. This indicates only little energy transfer.

The nonlinearity of effective local maximum potential shown in Fig. 5 is due to the applied potential value (+6 V) of each side electrode S1 and S2. However the curve shown in Fig. 5 could be approximated by two linear segments. The first segment has a slope of 1 and runs from $x = 3$ to $x = 9$ V, all potentials above $x = +3$ V applied on both tube electrodes potentials, cause maxima in the terminal stability regions, where negative ions can be trapped.

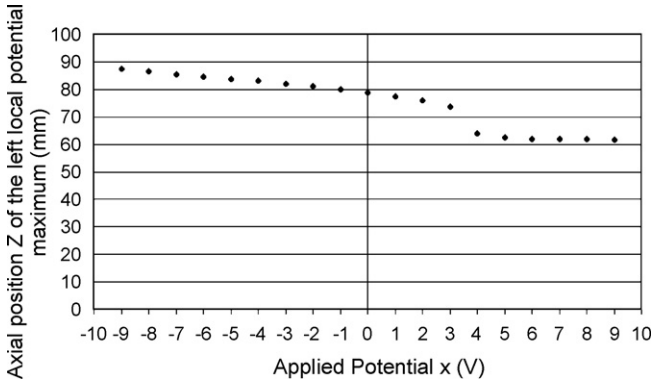

Fig. 6. Position of the left local maximum of the potential hill as a function of tube's potential x. At $z = 100$ mm there is a potential minimum.

The second segment covers the x range −9 to 0 V. Note that in this region potential maxima still exist even though the applied potential on each tube electrode reaches −9 V. This illustrates the role of side electrode potentials (+6 V), which have a great influence on establishing double hill configuration near the cell center. This still provides flat central stability region for trapping positive ions in the center of the ICR cell even for $x = -9$ V as shown in Fig. 3 before. Central well depth values are also shown in Fig. 5.

Fig. 6 shows the shift of potential maximum as a function of the applied potential x on each tube electrode. Local potential maximum of each potential hill shifts in the configuration x/6/0/6/x outward as x increases. This increases the distance between the two potential hills (as shown in Fig. 7) and thus trap negative ions more far away from the cell center. However, the curves shown in Figs. 6 and 7 are not linear. There is a point of inflection located between $x = 3$ and $x = 4$ V. Within this x transition, the sharp drop in the signal intensity of SF_6^- (Fig. 2) could also be experimentally observed.

So what happens in this narrow potential range? A strong shift in the local potential maximum of each potential hill out of the cell center accelerates the terminal negative ions axially outwards. By readjusting the potential of each tube electrode to return back from the transit configuration x/6/0/6/x (for $x > 3$) to 1/6/0/6/1 (as done in the experiments shown previously in Fig. 2)

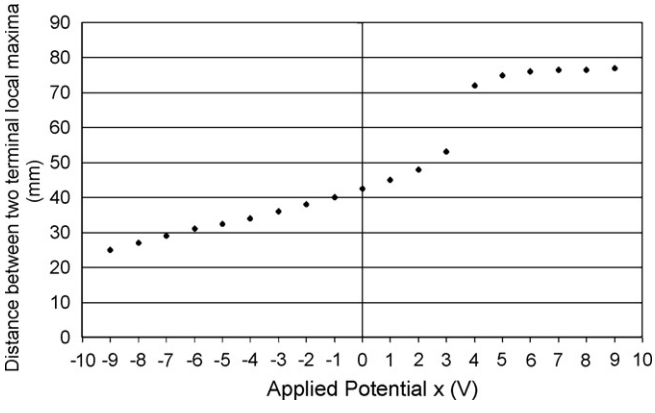

Fig. 7. Distance (mm) between the two potential hills in the double hill potential configuration x/6/0/6/x vs. x.

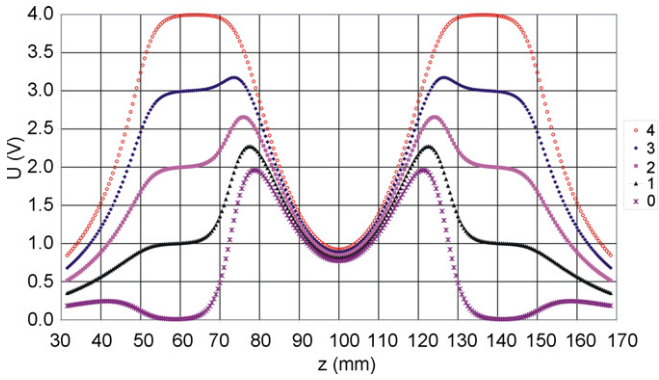

Fig. 8. Axial potential course in x/6/0/6/x potential configurations with x from 0 to +4 V.

the terminal negative ions, that were previously accelerated axially outwards gain a large acceleration magnitude toward the cell center. The translational energy of some negative ions along the z-axis (for applied tube potentials above $x = 3$ V) exceed the potential barrier in 1/6/0/6/1 at both terminal potential hills and they are ejected.

The loss of SF_6^- ions was experimentally observed at all x values higher than +3 V in Fig. 2. This corresponds to high shifts in the distance between the two terminal potential hills available as shown in Fig. 7. However, negative ions can be axially accelerated to outer regions during the potential change from 1/6/0/6/1 to x/6/0/6/x for $x = 2$ V and 3 V more than just indicated from the position of their corresponding potential hill maxima shown for $x = 2$ V and $x = 3$ V in Fig. 7 previously. An axial potential plot in x/6/0/6/x for $x = 0$ V to +4 V is shown in Fig. 8. This shows the reason, of using 1/6/0/6/1 and not 0/6/0/6/0 as an initial potential configuration for this study. The potential configuration 0/6/0/6/0 can trap positive ions in terminal regions A and E inside the tube electrodes, where no radial excitation and detection are possible. Furthermore, positive ions trapped in these extreme terminal regions cannot be extracted inwards toward the cell center, by applying whatever potential values on both tube electrodes R1 and R2 in the DAC potential range (from −9 to +9 V).

In order to avoid this problem, we have decided to use the configuration 1/6/0/6/1 as initial potential configuration. With this configuration, all positive ions generated directly from the pulsed electron beam outside the double potential hills are accelerated axially outwards and thus ejected from the cell (Fig. 8).

Negative ions in the transit potential configuration 2/6/0/6/2 are trapped at sharp unsymmetrical terminal potential hills. This asymmetry changes to form a shoulder, as the potential of each tube increases from +2 to +3 V. The large shift in the local potential maximum of the left hill along the transition from $x = 3$ to $x = 4$ V shown previously in Fig. 6 is due to the unsymmetrical form shown in Fig. 8.

3.1.2. SIMION calculations

Fig. 9 shows four trajectory calculations run by SIMION [24] program for 25 positive and 25 negative ion clouds trapped in the initial double hill potential configuration 1/6/0/6/1 for the

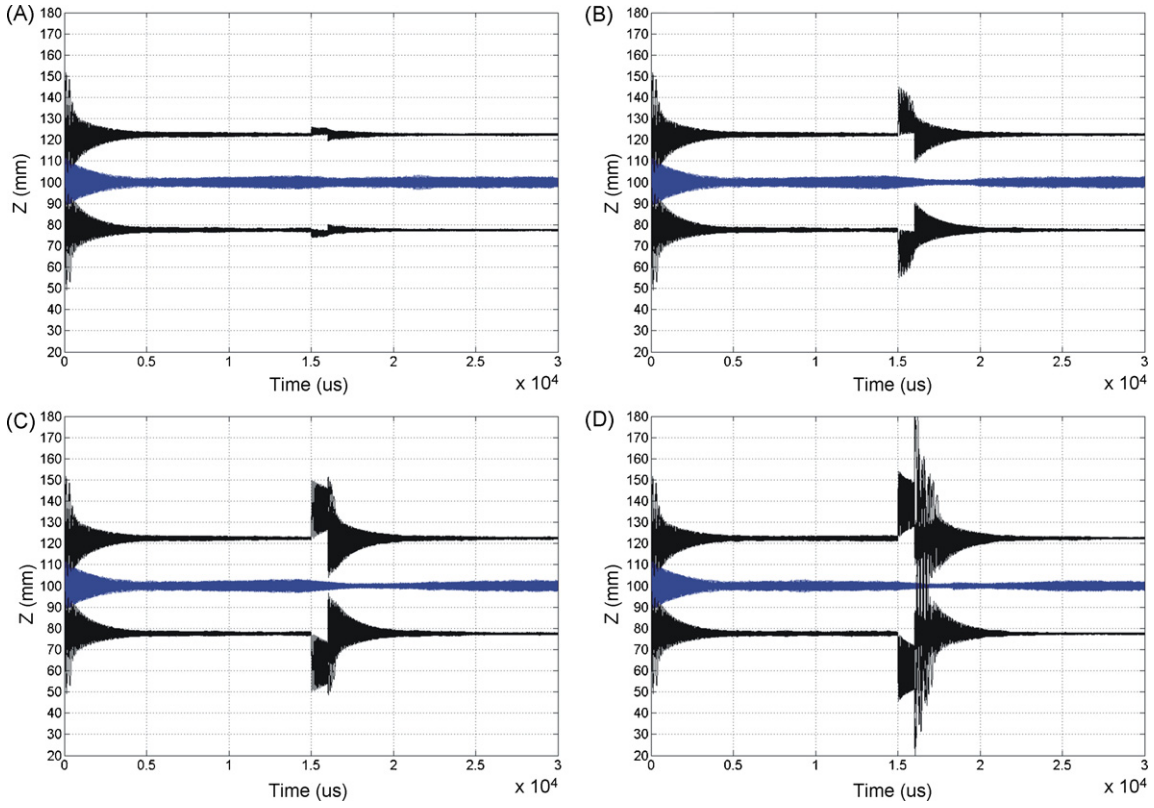

Fig. 9. SIMION simulations of 25 positive and 25 negative ion clouds at total columbic repulsion of 2×10^{-16} C and collisional damping constant of 1×10^{-3} during potential change from 1/6/0/6/1 to x/6/0/6/x. (A) $x = 2$ V, (B) $x = 3$ V, (C) $x = 4$ V and (D) $x = 9$ V. Positive ions are confined in the cell center, while negative ions are trapped on both terminal stability regions. All simulated positive ions are $m/z = 127$ and all negative ions are $m/z = 146$. Detection region is located between 70 and 130 mm.

first 15 ms. The potential of each tube electrode is changed (in phase) to x V exactly at TOF = 15 ms for just 1 ms duration. After that time, the potential of each tube is set up back (in phase) to +1 V. These simulations consider total columbic repulsion of 2×10^{-16} C and collision damping constant of 1×10^{-3}.

As indicated from Fig. 9(B), the potential change from 1/6/0/6/1 to 3/6/0/6/3 does not accelerate negative ions more than a few millimetres outward toward local potential maximum of the right potential hill at $z = 126.5$ mm (Fig. 8). This potential change increases the trapping amplitude of negative ions up to 145 mm on the left side (compare diagram B with diagrams A and C in Fig. 9). The outward directed gain in trapping amplitudes of accelerated terminal negative ions during potential change from 1/6/0/6/1 to x/6/0/6/x (with $x > +1$ V) is not linear as a function of the potential x of each tube electrode. This is also apparent when we compare diagrams A with B and C in Fig. 9. Furthermore negative ion trajectories are in different axial directions if we compare the forward potential change from $x = +1$ to higher potential values with the backward potential change from high potential values (>+1 V) to $x = +1$ V.

Higher transit potentials such as $x = 9$ V cause loss of negative ions. This was also observed experimentally before. Semiquantitative view concerning this negative ion loss can be discerned from the simulation in Fig. 9D and is shown in Fig. 10. Note that negative ion loss is not caused by the forward transition from $x = +1$ to $x = +9$ V but by the backward transition from $x = +9$ to $x = +1$ V.

Fig. 11 shows the nonlinearity in the degree of outward axial acceleration of terminal negative ions (represented as relative axial amplitude gains) during the forward potential transition from 1/6/0/6/1 to x/6/0/6/x for $x > +1$ V on both terminal potential hills. This was also shown in Fig. 9 as trajectory simulations for the cases $x = 2$, 3, 4, and 9 V in diagrams A, B, C and D, respectively. The existence of potential shoulders in the curves

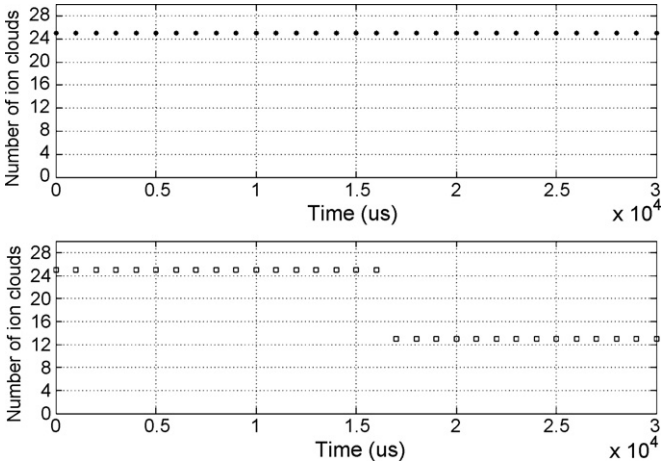

Fig. 10. Sudden negative ion loss (□) within the simulation shown in Fig. 9D as a result of a triggered (in phase) potential change of each tube electrode from +1 to +9 V at TOF = 15 ms for 1 ms duration. Number of positive ion clouds (●) remains unchanged.

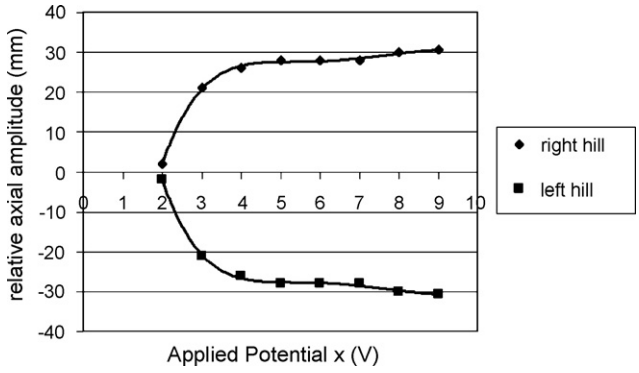

Fig. 11. Increase of axial trapping amplitude of terminal negative ions out of the cell relative to the trapping amplitude of negative ions at 1/6/0/6/1 as a function of the potential x of each tube electrode during the forward potential transition from 1/6/0/6/1 to x/6/0/6/x with $x > +1$ V. Fifth order trend lines connect the points.

corresponding to $x = +2$ and $x = +3$ V in Fig. 8 are responsible for this nonlinearity.

Fig. 12 shows inward axial anion acceleration during potential transition from 1/6/0/6/1 to x/6/0/6/x for $x = -3$, -4, -5, and -9 in diagrams A, B, C, and D, respectively. Inward axial motion of terminal negative ions is seen within time of flight range of 15–16 ms, where the corresponding transit potential configuration x/6/0/6/x applies. As shown from Fig. 12, no axial anion exchange occurs for transit potentials $x >= -3$ V of each tube electrode. However, even at $x = -9$ V, accelerated negative ions do not escape the cell axially after the end of the pulse at TOF = 16 ms as shown in diagram D in Fig. 12.

If we compare diagram D in Fig. 12 with diagram D in Fig. 9, we notice from the simulations, that axial kinetic energy gain for the case shown in diagram D in Fig. 12 is much lower than that in diagram D in Fig. 9 regardless of the fact that the acceleration direction between the two cases is opposite relative to each other. This difference in kinetic energy gain is due to the nonlinearity shown in Fig. 5 discussed above. Thus lower kinetic energy gain for terminal negative ions prevails even at very low tube potentials $x = -9$ V illustrated in diagram D in Fig. 12 during the potential transition from 1/6/0/6/1 to −9/6/0/6/−9. This ensures axial anion exchange and thus ion–ion collisions between central positive ions and inward-accelerated anions, without ejecting accelerated negative ions from the other side of the ICR cell. It should also be noted from the simulations, that this operation mode establishes anion–anion collisions too.

For $x = -4$ V and -5 V the simulations shown in diagrams B and C in Fig. 12, respectively, show positive-negative ion–ion axial contact. However, at these transit potentials, no noticeable drop in the signal intensity of SF_3^+ ions could be observed. This indicates, that SF_3^+ partial ion loss observed in Fig. 4 for lower transit potentials $x < -5$ V is not due to ion–ion neutralization reaction, but due to ion–ion collision between inwards-accelerated anions and stable central cations. It is the kinetic energy of the axially accelerated negative ions which determine, whether positive ions can still remain in their flat central stability region or not.

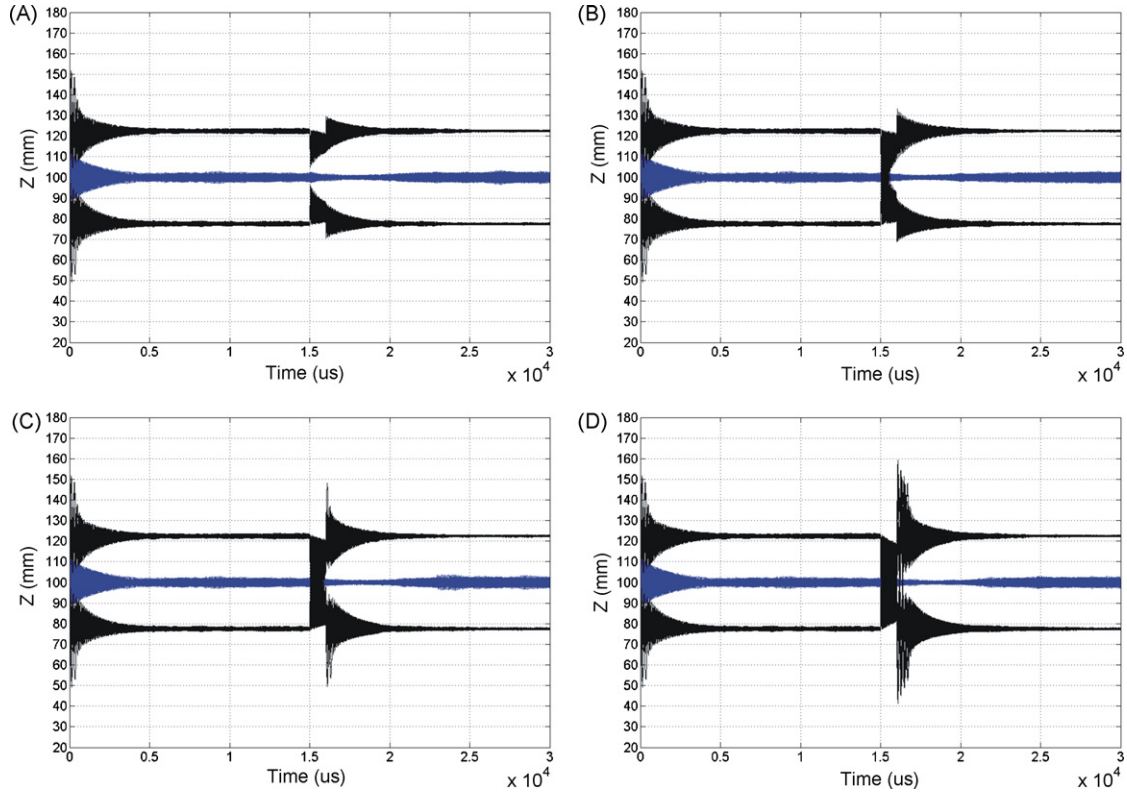

Fig. 12. SIMION simulations of 25 positive and 25 negative ion clouds at total columbic repulsion of 2×10^{-16} C and collisional damping constant of 1×10^{-3} during potential change from 1/6/0/6/1 to x/6/0/6/x. (A) $x = -3$ V, (B) $x = -4$ V, (C) $x = -5$ V and (D) $x = -9$ V. Positive ions are confined in the cell center, while negative ions are trapped on both terminal stability regions. All simulated positive ions are $m/z = 127$ and all negative ions are $m/z = 146$. Detection region 70–130 mm.

On the other hand, it should also be noted that SIMION simulations are not able to include ion–ion interaction such as SF_3^+ axial ion ejection observed experimentally in diagram B in Fig. 4 at transit potentials $x < -5$ V. This is due to the fact, that SIMION calculates fields using Laplace equation and not the more general Poisson equation. Although this program supports a number of charge repulsion estimates, here attractive interactions are discussed.

Thus we support the idea of partial axial positive ion ejection as the inwards-accelerated negative ions gain more translation energy along the z-axis, during the potential change from 1/6/9/6/1 to x/6/0/6/x for $x < -5$ V. This has been proven experimentally as indicated in diagram B in Fig. 4.

3.2. SIMION calculations of radial excitation pattern within the final potential configuration 1/6/0/6/1 and axial component of the radial excitation electric field

In all experiments done and shown in Section 3.1.1 previously, positive and negative ions were initially trapped in 1/6/0/6/1. A pulse of 1 ms duration was triggered to change the potential of each tube (in phase) from +1 to x V. After the end of this pulse, the potential of each tube was set up back to +1 V simultaneously. Now, a delay time of 100 ms duration allows for ion cooling through collision damping before a radial excitation pulse for detection was finally triggered. Thus, positive and negative ions were excited simultaneously for detection within the potential configuration 1/6/0/6/1. As a consequence, all simulations discussed later in this section will cover radial excitation events in the potential configuration 1/6/0/6/1.

Fig. 13 reveals a sharp discrimination of ion detection between central positive and terminal negative ions, as indicated with cyclotron radii differences after the end of a radial excitation pulse. Within this simulation, positive and negative ions underwent collisional cooling for the first 15 ms after ion generation, before a dipolar radial excitation pulse was triggered from the transmitter segments of the ring electrodes in resonance with the cyclotron frequency of SF_3^+ and SF_6^- (signal of two combined sine waves) for a duration of 100 μs.

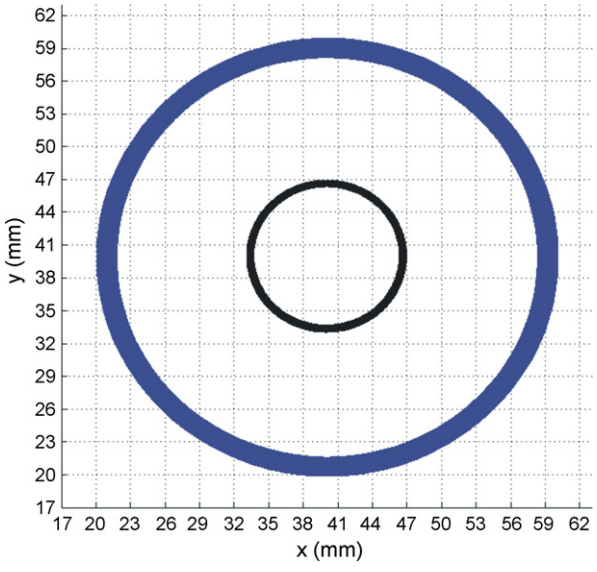

Fig. 13. SIMION simulation in the radial xy plane of positive (larger cyclotron radius) $m/z = 89$ and negative (smaller cyclotron radius) $m/z = 146$ ions after the end of radial excitation pulse for an additional 900 μs time of flight, during which ion collisional relaxation takes place (damping constant = 1×10^{-4}). Attenuation level of 0 db ($150.8 V_{p-p}$) for the radial excitation dipolar electric field was used. Sampling rate = 100 MHz.

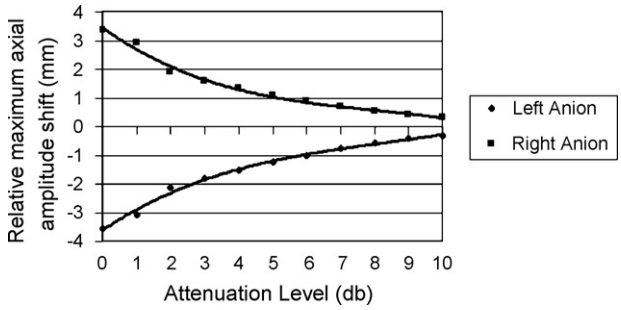

Fig. 14. Calculated relative maximum trapping amplitude of two terminal negative ions trapped in the static axial potential configuration 1/6/0/6/1 after the end of a radial dipolar excitation pulse, which is in-resonance with the cyclotron frequency of the simulated negative ions (with $m/z = 146$). Damping constant of 1×10^{-4} was used within this simulation. Radial excitation pulse duration = 100 μs.

The simulation was run for an additional 900 μs of time after the end of the dipolar excitation pulse to allow for collisional relaxation to be observed. m/z values of SF_3^+ and SF_6^- were used for the simulation. The ion polarities differ from each other not only in their final cyclotron radii at the end of the excitation pulse, but they differ also in their degree of relaxation within the same post excitation time interval (900 μs). So the amount of cyclotron radius decrease of central positive ion after the end of the radial excitation pulse is higher than that of terminal SF_6^- ions. Radial ion discrimination is discussed in detail elsewhere [23].

Fig. 14 shows the shift of maximum trapping amplitude of two terminal negative ions after the trigger of the radial excitation pulse as a function of attenuation level of the radial dipolar excitation pulse. The peak to peak voltage of the radial excitation pulse is related to the attenuation level (X_A) by the equation: $V_{p-p} = 150.77 \exp(-0.1334 X_A)$. These axial shifts were calculated relative to the maximum normal z-amplitudes of these two terminal negative ions ($m/z = 146$), when no radial excitation pulse was applied.

It is clear to see from Fig. 14, that the shift of maximum axial amplitude of terminal negative ions is not dominant in a specific strength range of the radial excitation electric field. However, this shift is more intensive below 5 db (above $77.4 V_{p-p}$), where negative ion radius becomes high enough to escape the axial interfering electric field of the terminal tubes (with radius of 5 mm) and to enter a new axial electric field of the terminal side electrodes ($r > 5$ mm).

Ions with different polarities can be accelerated differently in radial direction by the dipolar radial excitation electric field. To study these differences in ion radial acceleration, one central positive ion $m/z = 89$ and one terminal negative ion $m/z = 146$ were simulated in the potential configuration 1/6/0/6/1 at damp-

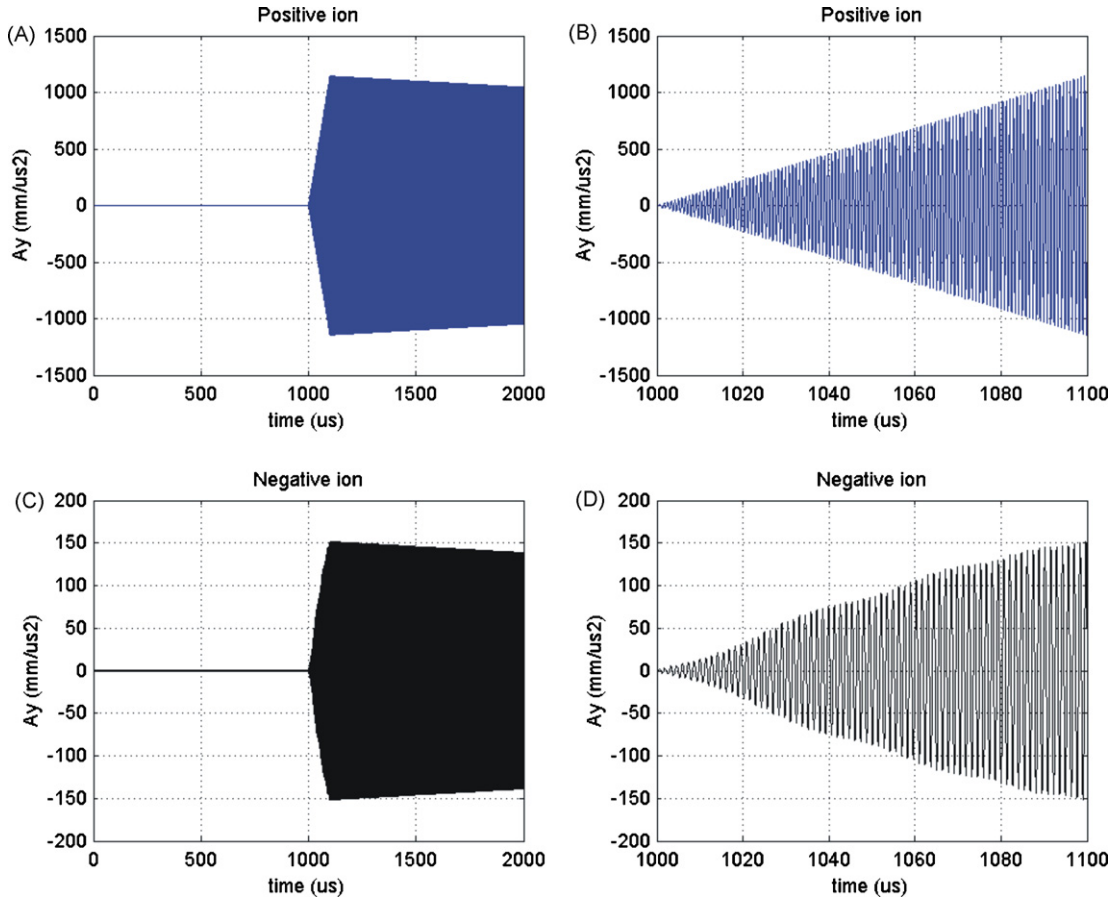

Fig. 15. Radial acceleration component in y direction (mm/μs^2) of positive SF_3^+ ions (diagrams A and B) and negative SF_6^- ions (diagrams C and D) as a function of time in the applied potential configuration 1/6/0/6/1. For details about simulation parameters see text. Diagrams B and D are enlarged views of diagrams A and C, respectively.

ing constant of 1×10^{-4}. Thermally initiated positive and negative ions (kinetic energy = 4×10^{-2} eV along the z-axis) were let to cool down axially for just 1000 μs before a radial excitation pulse with attenuation level of 0 db was triggered only for 100 μs. After this duration, ions were observed in their collisional relaxation period between 1100 and 2000 μs. No potential change of tube's electrodes or side electrodes was done during this simulation, so that only 1/6/0/6/1 static potential configuration was dominant. No ion repulsion estimations were used.

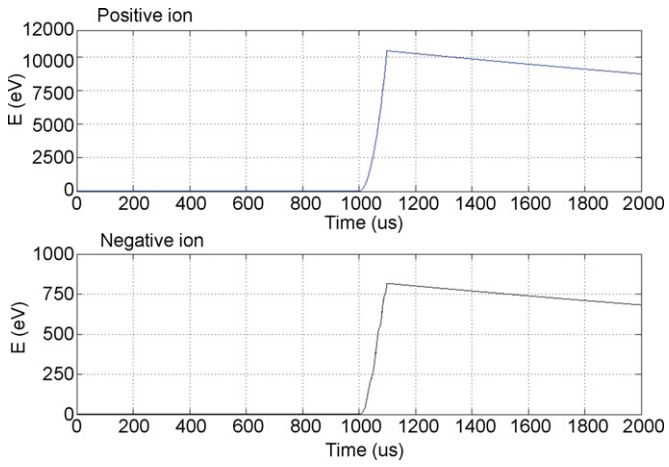

Fig. 16. Kinetic energy as a function of time for central positive (SF_3^+) and terminal negative SF_6^- ions in the potential configuration 1/6/0/6/1.

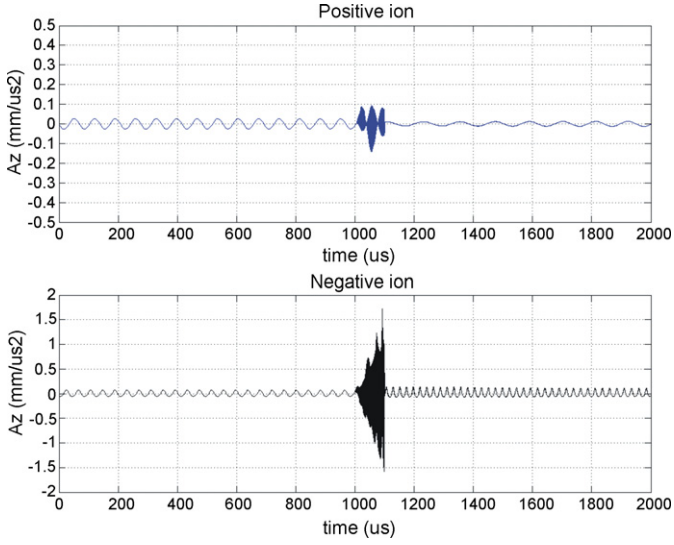

Fig. 17. Axial component of acceleration (mm/μs^2) for central positive and terminal negative ions as a function of time.

After the end of the radial excitation pulse, the central positive ion radial acceleration is 1150 mm/μs^2, while the terminal negative ion gains 150 mm/μs^2 only. Thus, terminal negative ions can be accelerated by just 13% relative to the radial acceleration amount of central positive ions. Furthermore, there is a noticeable nonlinearity in the time dependent radial acceleration component of terminal negative ion (compare diagrams D with B in Fig. 15).

The difference in radial acceleration magnitude of positive and negative ions, trapped in different stability regions has a strong effect on the post-excitation total kinetic energy gain as shown in Fig. 16. As central positive ion can be accelerated to 10.5 keV (at relatively high damping constant of 1×10^{-4} and homogeneous magnetic field of 7 T) using radial excitation pulse of 150.8V_{p-p} (0 db), terminal negative ion can only gain 820 eV of kinetic energy at the same conditions.

On the other hand, radial energy dissipation is dominant in both ion polarities, since an axial acceleration component exists during radial excitation event (Fig. 17). However, axial acceleration component is greater in negative ion case and this also contributes to the limitation applied on the increase of negative ion's cyclotron radius during radial excitation in comparison with that of central positive ion. Fig. 17 reveals more useful information. The axial acceleration component of the central positive ion decreases in frequency and magnitude after radial excitation. On the other hand, axial component of acceleration increases in frequency and magnitude in the case of a negative ion trapped in a terminal stability region at the same conditions. The noticeable decrease in the frequency and magnitude of the axial component of acceleration of central positive ion indicates a lower effective trapping electric field at the specified cyclotron radius, that the positive ion reaches after radial acceleration (with attenuation level of 0 db in this case).

We notice in case of SF_3^+ radial excitation a small perturbation in the axial acceleration component of central positive ion during radial excitation event (Fig. 17), although the equipoten-

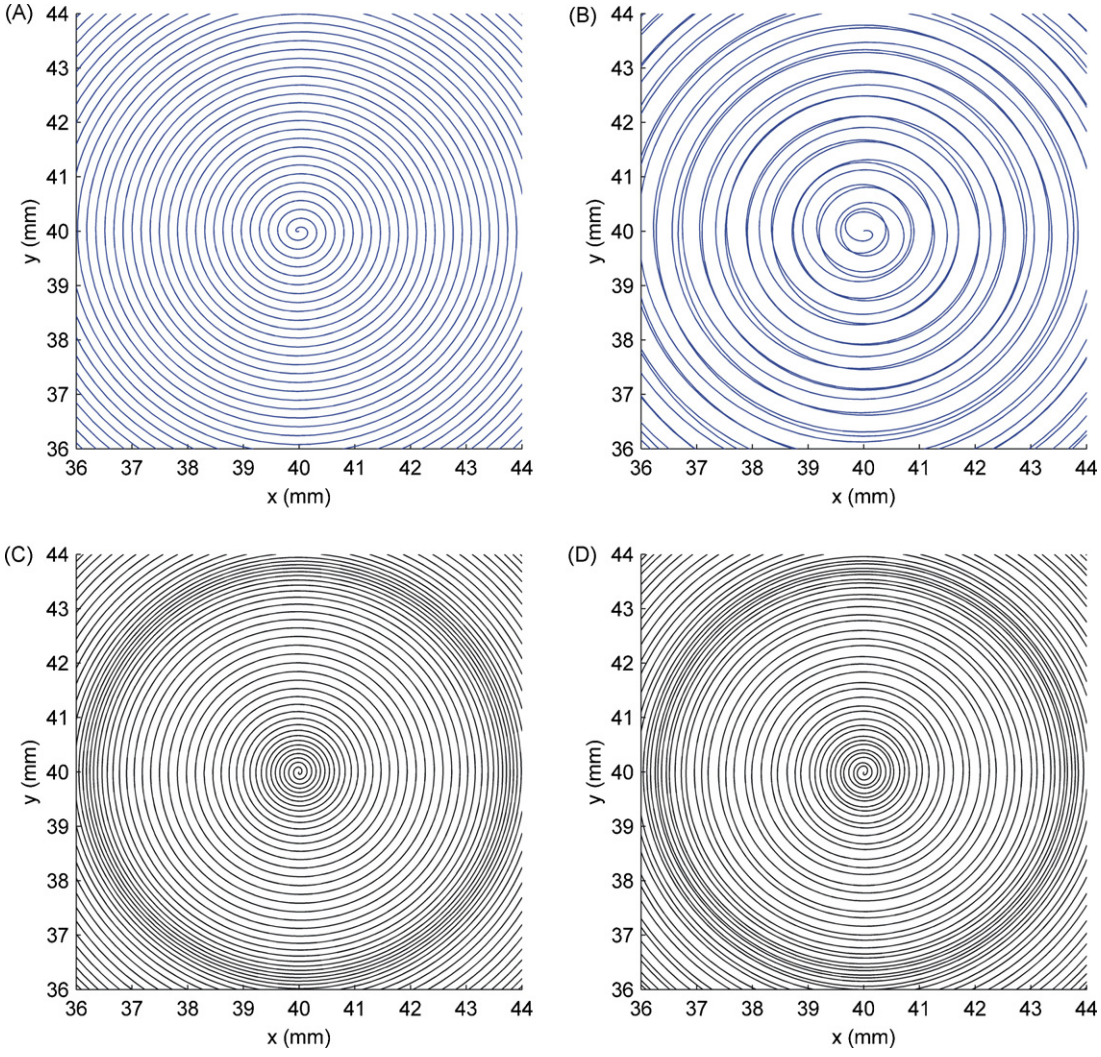

Fig. 18. Enlarged radial *xy*-views of positive and negative ions during radial excitation. (A) Pure radial excitation of one central positive ion at $m/z = 89$ (no on resonance RF-frequency for negative ions was transmitted). (B) Radial excitation of the same central positive ion, but with a combined RF cyclotron frequency for simultaneous excitation of both ion polarities SF_3+ and $SF6^-$. (C) Pure radial excitation of one terminal negative ion at $m/z = 146$ (no on resonance RF-frequency for positive ions was transmitted). (D) Radial excitation of the same terminal negative ion, but with a combined RF cyclotron frequency for simultaneous excitation of both ion polarities SF_3^+ and SF_6^-.

tial lines (not shown) of radial excitation electric field at 0 db are nearly parallel to each other in the central region of the ICR cell. This perturbation is due to the influence of the second RF-frequency triggered to excite negative ions simultaneously with positive ions. Fig. 18 illustrates the net effect of the distortion of ion trajectories during radial ion excitation of both ion polarities. The co-transmission of another cyclotron frequency during simultaneous excitation of both SF_3^+ and SF_6^- influences ion trajectories of both ion polarities. However, the influence of transmitting resonant RF-frequency for exciting SF_6^- together with SF_3^+ on the ion trajectory of SF_3^+ is greater than the influence of transmitting resonant RF-frequency for exciting SF_3^+ together with SF_6^- on the ion trajectory of SF_6^- (compare diagrams A and B relative to diagrams C and D in Fig. 18).

Furthermore, the increase of cyclotron radius of terminal SF_6^- ion is nonlinear in both cases C and D as a function of time. This is due to the nonlinearity in the increase of the radial acceleration component in the terminal stability regions as shown previously in Fig. 15.

4. Conclusion

Both positive and negative ions can be trapped and detected simultaneously in a static double hill potential configuration in this new ICR cell. Axial potential distributions reveal asymmetric terminal stability regions relative to a symmetrical central region. Anion–anion spatial exchange could be achieved by a new operation mode, which implies changing the potential of each tube electrode in a specific potential range. Single axial pulse experiments described in this paper delivered experimental evidence of ion–ion interactions. SIMION simulations also imply that anion–anion collisions are possible. The axial component of the radial excitation electric field exists in the terminal stability regions and plays a role in dissipating kinetic energy during radial excitation. A sharp discrimination in radial dipolar excitation between positive and negative ions is shown. In depth analysis of ion dynamics and electric potential distribution patterns provides explanations to the observations. Distortion in radial ion trajectories could be noticed when both ion polarities were excited simultaneously in radial direction.

Acknowledgements

B. Kanawati would like to thank VCI (Verband der Chemischen Industrie) for a PhD grant. We also thank Mr. Wolfgang Fulda and his coworkers of the mechanical shop for building the new ICR cell and for providing continuous mechanical support.

References

[1] A.G. Marshall, C.L. Hendrikson, G.S. Jackson, Mass Spectrom. Rev., 17 (1998) 1.
[2] B. Kanawati, K.P. Wanczek, Int. J. Mass Spectrom. 264 (2007) 164.
[3] S. Fornarini, Mass Spectrom. Rev. 15 (1996) 365.
[4] K.P. Wanczek, Z.C. Profous, Int. J. Mass Spectrom. Ion Processes 17 (1975) 23.
[5] S. Guan, M.C. Wahl, T.D. Wood, A.G. Marshall, Anal. Chem. 65 (1993) 1753.
[6] J.P. Speir, G.S. Gorman, C.C. Pitsenberger, C.A. Turner, P.P. Wang, I.J. Amster, Anal. Chem. 65 (1993) 1746.
[7] C.L. Hendrickson, D.A. Laude, Anal. Chem. 67 (1995) 1717.
[8] S.E. Barlow, M.D. Tinkle, Rev. Sci. Instrum. 73 (2002) 4185.
[9] G. Gabrielse, L. Haarsma, S.L. Rolston, Int. J. Mass Spectrom. 88 (1989) 319.
[10] W.W. Yin, M. Wang, A.G. Marshall, E.B. Ledford, J. Am. Soc. Mass Spectrom. 3 (1992) 188.
[11] S. Guan, A.G. Marshall, Int. J. Mass Spectrom. 146/147 (1995) 261.
[12] G. Bollen, S. Becker, H.-J. Kluge, M. König, R.B. Moore, T. Otto, H. Raimbault-Hartmann, G. Savard, L. Schweikhard, Nucl. Instrum. Methods A 368 (1996) 675.
[13] D. Beck, F. Ames, G. Audi, G. Bollen, F. Herfurth, H.-J. Kluge, A. Kohl, M. König, D. Lunney, I. Martel, R.B. Moore, H. Raimbault-Hartmann, E. Schark, S. Schwarz, M.D. Simon, J. Szerypo, Eur. Phys. J. A 8 (2000) 307.
[14] Y. Wang, K.P. Wanczek, Rev. Sci. Instrum. 64 (1993) 883.
[15] V.H. Vartanian, D.A. Laude, Org. Mass Spectrom. 29 (1994) 692.
[16] R. Malek, K.P. Wanczek, Int. J. Mass Spectrom. 157/158 (1996) 199.
[17] R. Malek, K.P. Wanczek, Rapid Commun. Mass Spectrom. 11 (1997) 1616.
[18] M.V. Gorshkov, S. Guan, A.G. Marshall, Rapid Commun. Mass Spectrom. 6 (1992) 166.
[19] V. Frankevich, R. Zenobi, Int. J. Mass Spectrom. 207 (2001) 57.
[20] R.E. March, J.F. Todd, Quadrupole Ion Trap Mass Spectrometry, Wiley–Interscience, second ed., 2005, ISBN-10: 0471488887.
[21] G. Gabrielse, S.L. Rolston, L. Haarsma, Phys. Lett. A 129 (1988) 38–42.
[22] R.A. Zubarev, N.L. Kelleher, F.W. McLafferty, J. Am. Chem. Soc. 120 (1998) 3265.
[23] B. Kanawati, K.P. Wanczek, Rev. Sci. Instrum. 78 (2007) 074102.
[24] D.A. Dahl, Idaho National Engineering and Environmental Laboratory, Idaho Falls 83415, ID.